MATERIALS SCIENCE

Bilateral alkylamine for suppressing charge recombination and improving stability in blade-coated perovskite solar cells

Wu-Qiang Wu, Zhibin Yang, Peter N. Rudd, Yuchuan Shao, Xuezeng Dai, Haotong Wei, Jingjing Zhao, Yanjun Fang, Qi Wang, Ye Liu, Yehao Deng, Xun Xiao, Yuanxiang Feng, Jinsong Huang*

The power conversion efficiencies (PCEs) of perovskite solar cells (PSCs) are already higher than that of other thin film technologies, but laboratory cell-fabrication methods are not scalable. Here, we report an additive strategy to enhance the efficiency and stability of PSCs made by scalable blading. Blade-coated PSCs incorporating bilateral alkylamine (BAA) additives achieve PCEs of 21.5 (aperture, 0.08 cm^2) and 20.0% (aperture, 1.1 cm^2), with a record-small open-circuit voltage deficit of 0.35 V under AM1.5G illumination. The stabilized PCE reaches 22.6% under 0.3 sun. Anchoring monolayer bilateral amino groups passivates the defects at the perovskite surface and enhances perovskite stability by exposing the linking hydrophobic alkyl chain. Grain boundaries are reinforced by BAA and are more resistant to mechanical bending and electron beam damage. BAA improves the device shelf lifetime to >1000 hours and operation stability to >500 hours under light, with 90% of the initial efficiency retained.

INTRODUCTION

Perovskite solar cells (PSCs) show great potential for future commercialization due to their mounting power conversion efficiencies (PCEs) and compatibility with simple low-temperature solution processing that has cost advantages and promise of device scaling up (*1*–*4*). Early efforts to bring this emerging technology from the laboratory to the market have witnessed impressive progress, such as the one-step blade-coating technique combined with composition/surfactant/dopant-engineering strategies to achieve uniform and large-area perovskite film coating, improve device performance, and simplify device architecture (*5*–*7*). A certified efficiency of 15% for a 57-cm^2 module was achieved by fast blade coating at an unprecedented speed of 180 m hr^{-1} (efficiency was certified by Newport after the publication of the paper) (*6*). However, commercialization of a perovskite-based photovoltaic technology requires further advancement in both efficiency and long-term stability, with low-cost materials and ease of printability.

High-quality perovskite films are critical to realize highly efficient and stable PSCs (*8*–*10*). However, polycrystalline perovskite films inevitably contain a high density of crystallographic defects, such as uncoordinated ions and dangling bonds at surfaces and grain boundaries, which can result in charge recombination via nonradiative channels, and thus impair device performance (*11*–*13*). On the other hand, organic-inorganic hybrid perovskites, e.g., $CH_3NH_3PbI_3$, are unstable under high moisture, illumination, or heat due to their soft nature, i.e., low interaction energy between metal cations and halide anions induces a high density of ionic defects and volatility of the organic cations (*14*, *15*). All of these aspects impose challenges for long-term deployment of PSCs in the field.

Previous studies have demonstrated strategies of introducing additional functional layers on top of perovskite layers to either passivate the surface defects or improve the ambient stability of perovskite films (*11*, *16*–*19*). Although promising, it is more desirable to directly formulate the perovskite inks to avoid an additional step during the scalable fabrication of PSCs. Ink formulation engineering has been established in spin-coated devices to viably modulate crystal growth, passivate defects, and form a protection barrier for improved efficiency and stability via several types of additives, such as small organic molecules (*20*, *21*), ammonium salts (*22*–*24*), long-chain polymers (*25*–*27*), and ionic liquids (*28*). However, multifunctional additives that are judiciously designed for blade-coated perovskite films are still lacking; the reported molecules are found to not function as well because of the different film formation mechanism in the blade-coating process. There is a dilemma in the utilization of some additives to smooth bladed perovskite films because the additives often promote the formation of small grains and thus increase the area of grain boundaries.

Here, we demonstrate that simple tailoring of the perovskite ink formulation with a small amount of bilateral alkylamine (BAA) additive, i.e., molecules with a structure of "$NH_2—R—NH_2$," not only helps in constructing compact perovskite films with uniform size distribution and fewer pinholes but also has strong capability to passivate the perovskite grain surface. This BAA-incorporated strategy results in significantly enhanced efficiency and stability of p-i-n–structured PSCs without adding complexity to the scalable fabrication process. One example of the effectiveness of this strategy is that the stabilized open-circuit voltage (V_{oc}) of the bladed methylammonium lead iodide ($MAPbI_3$) devices by BAA passivation was enhanced to 1.18 V, which is well above those counterparts made by spin coating.

RESULTS

Ink formulation and film formation

A series of BAA additives were studied in this work, featuring a three-, six-, or eight-carbon chain with $—NH_2$ tails at both ends, i.e., 1,3-diaminopropane (DAP), 1,6-diaminohexane (DAH), and 1,8-diaminooctane (DAO). The chemical structures of the different BAA additives are shown in Fig. 1A. BAAs, with symmetric molecular

---

Department of Applied Physical Sciences, University of North Carolina, Chapel Hill, NC 27599, USA.
*Corresponding author. Email: jhuang@unc.edu

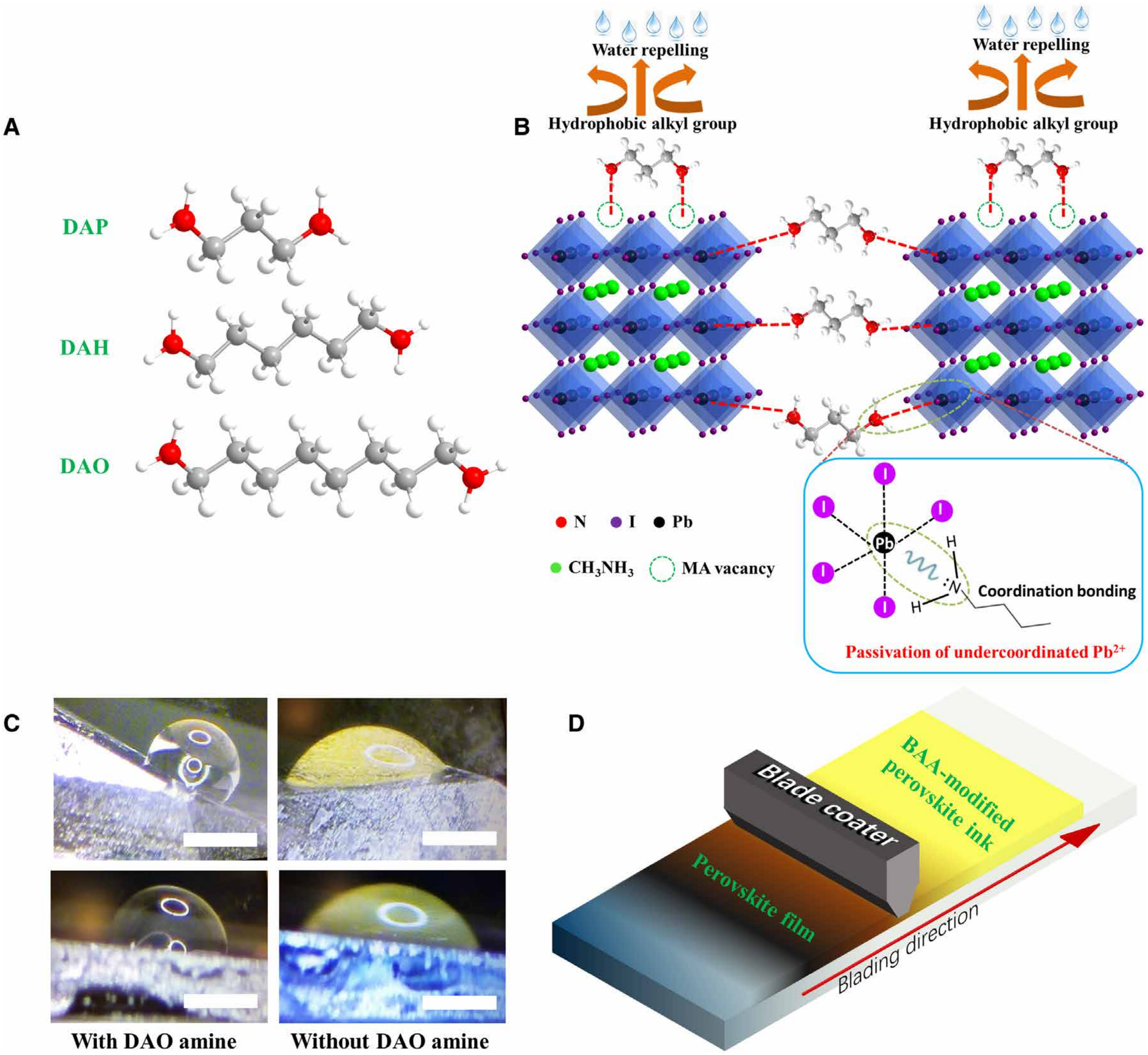

Fig. 1. Chemical structures and functions of BAA additives, contact angle measurement, and blading process. (**A**) Chemical structures of BAA additives. (**B**) Schematic illustration of defect passivation and water repellence induced by BAA incorporation. (**C**) Contact angle measurement of a water droplet on $MAPbI_3$ single crystals (top row) and $MAPbI_3$ thin films (bottom row) with or without incorporated BAA additive. Scale bars, 5 cm. (**D**) Sketch showing the blade-coating process for the perovskite film.

structure, comprise hydrophilic amino tails at both ends and a hydrophobic alkyl chain core. Furthermore, BAAs are commercially available liquids at room temperature. They can be dissolved in water, most polar solvents, and more significantly, all known solvents for perovskites. The three BAAs were chosen with the objective of passivating crystallographic defects at the perovskite grain surface by forming coordination bonds between undercoordinated Pb^{2+} ions and $-NH_2$ tails, as shown schematically in Fig. 1B. In addition, the $-NH_2$ tails can occupy A-site vacancies at $MAPbI_3$ grain surface. Superior to regular amine molecules, BAAs tend to anchor onto the perovskite grain surface with both $-NH_2$ tails, which exposes the linking hydrophobic carbon chain and forms a moisture-repelling barrier on $MAPbI_3$ grains. This is evidenced by the increased contact angle of water droplets on BAA-modified perovskite films or single crystals, as shown in Fig. 1C. The BAA-modified perovskite films become water insoluble despite both DAP and perovskites being very soluble in water. This indicates very strong bonding of both $-NH_2$ tails to the perovskite. In contrast, control perovskite films quickly dissolved, coloring the water droplets yellow.

The perovskite films were prepared by blade coating a BAA-incorporated perovskite ink over a preheated indium tin oxide (ITO) glass substrate (*7*), as illustrated in Fig. 1D. The BAA molecules have low boiling points; hence, it was examined whether the BAA molecules remained in the perovskite films after annealing. DAP was used as a representative BAA additive to study its possible interaction with $MAPbI_3$ and influence on the perovskite film formation. Fourier transform infrared (FTIR) spectra in fig. S1 indicate that the primary amine analog was still present within the bladed perovskite films after annealing at relatively high temperatures. Since DAP is a liquid at room temperature, logically, there must be a strong interaction between DAP and perovskites that keeps DAP in the perovskite films after high-temperature annealing. However, the thickness of the DAP layer should be self-limited to a monolayer on perovskites because the interaction between DAP molecules is too weak to keep them in solid form. Moreover, the strong interaction of DAP molecules with $MAPbI_3$ precursors slows the crystallization and formation of $MAPbI_3$ films. Before annealing, the formed $MAPbI_3$ film with only 0.025 weight % (wt %) DAP additive in the ink solution retained x-ray diffraction (XRD) amorphous characteristics, while the pure $MAPbI_3$ film showed distinct peaks (fig. S2). It is speculated that DAP functions as a Lewis base due to its amino groups, with coordination bonds formed by sharing the lone electron pair at N atom with the empty 6p orbit of Pb^{2+} (*25*, *29*, *30*). This coordination bonding could retard the reaction of methylammonium iodide (MAI) and PbI_2, as suggested by the reduced grain size of DAP-modified $MAPbI_3$ thin films with increasing amounts of DAP (fig. S3). Nevertheless, the slower crystallization enabled the formation of highly uniform and compact perovskite films, thus reducing the device leakage current (*25*).

To determine whether DAP molecules get into the crystal structure of $MAPbI_3$, we analyzed XRD patterns of $MAPbI_3$ films after annealing with different DAP concentrations (0 to 0.05 wt %) in the perovskite inks. As shown in fig. S4, all observed XRD reflections were indexed as $MAPbI_3$ characteristic peaks (*31*). There is no noticeable shift of peaks toward lower angles, indicating no significant unit cell expansion in the perovskite lattice or incorporation of DAP into the $MAPbI_3$ crystal structure (*24*, *32*). Because of the large molecular size of DAP, the amine additives prefer to stay at the periphery of the perovskite grains, with $-NH_2$ terminal groups limited to interacting with undercoordinated Pb ions exposed at the surface.

The $MAPbI_3$-DAP film (0.025 wt % DAP) showed a more uniform and compact microstructure, with ultrafine grains and a smooth surface, compared with the control $MAPbI_3$ film (Fig. 2, A to D). The control film had a grain size of approximately 300 to 500 nm and a root mean square (RMS) surface roughness of 31.1 nm from atomic force microscopy (AFM) scanning (fig. S5). DAP modification decreased the grain size to approximately 100 to 300 nm and reduced RMS surface roughness to 24.9 nm. The improved uniformity and smoothness of the bladed perovskite films was attributed to DAP modulating the crystallization of $MAPbI_3$. Specifically, the bilateral $-NH_2$ groups strongly interact with neighboring $MAPbI_3$ grains and link them together, which may force the crystals to grow in contact with each other more tightly. To examine how DAP reinforces the grain boundaries, we subjected the perovskite films to mechanical stress and electron beam damage testing. Films were fabricated on flexible ITO/PET (ITO films on polyethylene terephthalate) substrates and then bent into a curved shape with a radius of 1 cm for several cycles. As shown in Fig. 2 (E to G), the $MAPbI_3$-DAP film remained intact after bending, while a lot of pinholes were generated in the control $MAPbI_3$ film. The cracks after bending generally appear at grain boundaries under tensile strain along the plane direction. The improved tolerance of film bending should be mainly caused by the bridging of neighboring grains by the DAP additives with two $-NH_2$ tails, which act as a glue between grains. In addition, the weak interaction between perovskites and the underlying poly(triaryl amine) (PTAA) layer may cause the peeling of the perovskite grains and result in the generation of pinholes, as shown in Fig. 2F. The $-NH_2$ functional group of DAP can participate in hydrogen bonding with the underlying PTAA layer to improve adhesion between perovskite and hole transport layer (HTL), thus reducing the peeling-off possibility of the perovskite film during bending. Overall, the correlation between a strengthened passivation of grain boundaries and a more compact film with fewer pinholes after bending is due to reinforced molecular bonding between DAP, perovskite, and the underlying layer. It is known that an electron beam can damage perovskites, and cracks are often generated first at grain boundaries (*33*, *34*). We used a high-energy electron beam with a voltage of 1 kV and a current of 15 μA under scanning electron microscopy (SEM) to accelerate degradation of grain boundaries (note that the settings are much higher than required for regular SEM observations). As seen in Fig. 2H, the control $MAPbI_3$ film exhibited obvious cracks after the sixth consecutive scan (the observed area was exposed for approximately 15 s per scan), while the $MAPbI_3$-DAP film retained dense grain packing even after exposure to the high-energy electron beam. This

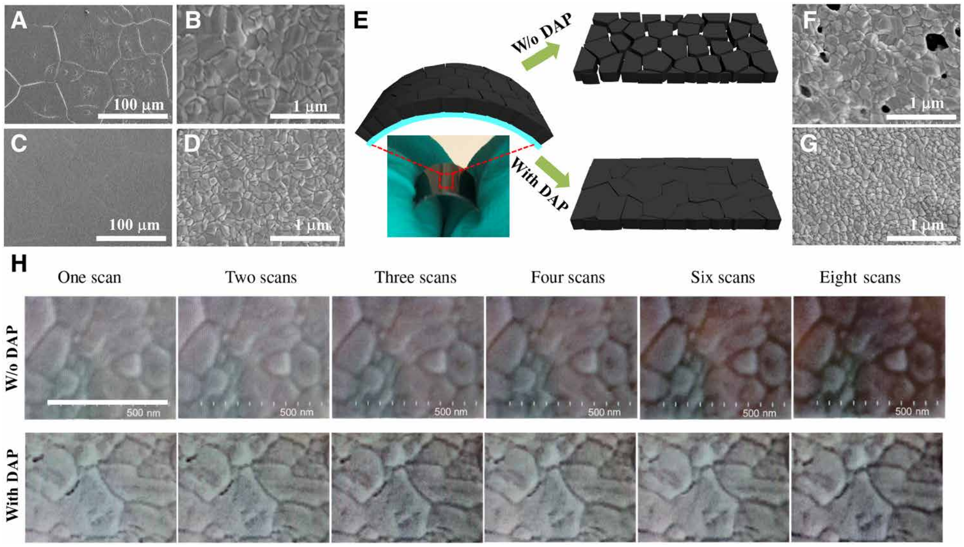

Fig. 2. Perovskite film morphologies and mechanical test. Surface SEM images of (**A** and **B**) $MAPbI_3$ and (**C** and **D**) $MAPbI_3$-DAP (0.025 wt % DAP added). (**E**) Sketch showing the morphology change of the perovskite films deposited on a flexible ITO-PET substrate after the bending test. Corresponding SEM images of (**F**) $MAPbI_3$ and (**G**) $MAPbI_3$-DAP films after bending. (**H**) SEM images showing the degradation of grain boundaries for $MAPbI_3$ and $MAPbI_3$-DAP films after exposure to the high energy electron beam for several scanning cycles during SEM characterization. Scale bar, 500 nm (H).

comparison indicates that DAP reinforces grain boundaries, which are the weakest spots in polycrystalline perovskite films. In addition, $MAPbI_3$-DAP devices had greatly reduced dark current or leakage current densities compared to $MAPbI_3$ cells (fig. S6), again confirming the compactness of the $MAPbI_3$-DAP films. The energy levels of $MAPbI_3$ films prepared in the absence or presence of DAP were studied by ultraviolet (UV) photoelectron spectroscopy. Overall, the energy levels were negligibly changed upon incorporation of very low concentrations of DAP, i.e., 0.025 wt % (fig. S7 and table S1).

Photovoltaic performances

We fabricated PSCs with the inverted p-i-n structure using perovskite films with or without DAP additives (Fig. 3A). A typical PSC was assembled with a structure of ITO/PTAA/BAA-modified perovskite/C_{60}/bathocuproine (BCP)/Cu, where an approximately 500-nm-thick homogeneous and pinhole-free perovskite film (fig. S8) was sandwiched between the HTL of PTAA and the electron transport layer (ETL) of C_{60}, featuring a planar heterojunction configuration. The photovoltaic performances of the PSCs based on $MAPbI_3$ films incorporated with different amounts of DAP are summarized in table S2. The optimal DAP additive concentration was 0.025 wt %. Less DAP content caused insufficient passivation, while excess DAP in $MAPbI_3$ resulted in a worse film morphology, which can be ascribed to aggregated DAP molecules impairing perovskite crystal growth (fig. S3) (*24*). The *J-V* curves of the PSCs with and without DAP are shown in Fig. 3B, while the extracted device parameters are summarized in Table 1. The PSCs based on the pristine $MAPbI_3$ thin film showed a typical PCE of 18.3% with a short-circuit density (J_{sc}) of 22.0 mA cm^{-2}, a V_{oc} of 1.08 V, and a fill factor (FF) of 77.2%. For the $MAPbI_3$-DAP device, the PCE increased to 21.7%, while the V_{oc} and FF were significantly enhanced to 1.18 V and 81.7%, respectively. It is worth noting that the optimal concentration for all three BAA additives (i.e., DAP, DAH, and DAO) is the same, namely, 0.025 wt %, and the DAP-incorporated PSC showcased the best performance (a PCE of 21.7%) when compared with DAH-based device (a PCE of 20.8%) or DAO-based cell (a PCE of 20.3%), which can be attributed to the moderate length of carbon chain in DAP for an optimized interaction with perovskite films. During the film formation, the DAP can be expelled to the film surface. A carbon chain that is too long will impair the charge transport from perovskite to ETL. Hence, the carbon chain length optimization of universal BAA additive is also a critical factor to balance the defect passivation and charge collection and thus effectively improving the device performance. For PSCs based on $MAPbI_3$-DAP films, a negligible photocurrent hysteresis has been observed (fig. S9 and table S3). The suppressed photocurrent hysteresis in the $MAPbI_3$-DAP–based PSC was attributed to the effective passivation and/or stabilization of undercoordinated ions at the surface of the perovskite crystals through strong molecular interaction with $-NH_2$ functional groups. To confirm this, lateral structured devices were fabricated with two parallel Au finger electrodes deposited on top of glass/$MAPbI_3$ and glass/$MAPbI_3$-DAP films. When a voltage pulse (17.5 V) was applied, the current of the latter device immediately increased to the maximum, while the former device needed 1200 s to stabilize the current, suggesting that trap passivation and ion migration suppression resulted from DAP incorporation (fig. S10).

The universality of the BAA passivation was examined by adding the DAP additive to perovskite inks of different compositions and bandgaps ranging from 1.51 to 1.82 eV (Fig. 3B and Table 1). Enhanced V_{oc}, FF, and device performance were observed for all tested perovskite compositions containing DAP. This result highlights the effectiveness and versatility of using the BAAs for defect passivation and performance enhancement. The PSCs based on Cs/FA/MA mixed-cation perovskite (CFM) with DAP passivation [an optical bandgap of 1.51 eV, determined from the external quantum efficiency (EQE) spectrum edge of 821 nm in fig. S11] had a high V_{oc} of 1.16 V, corresponding to a record low V_{oc} deficit of 0.35 V. To the best of our knowledge, this is the smallest deficit value for all PSC devices reported so far.

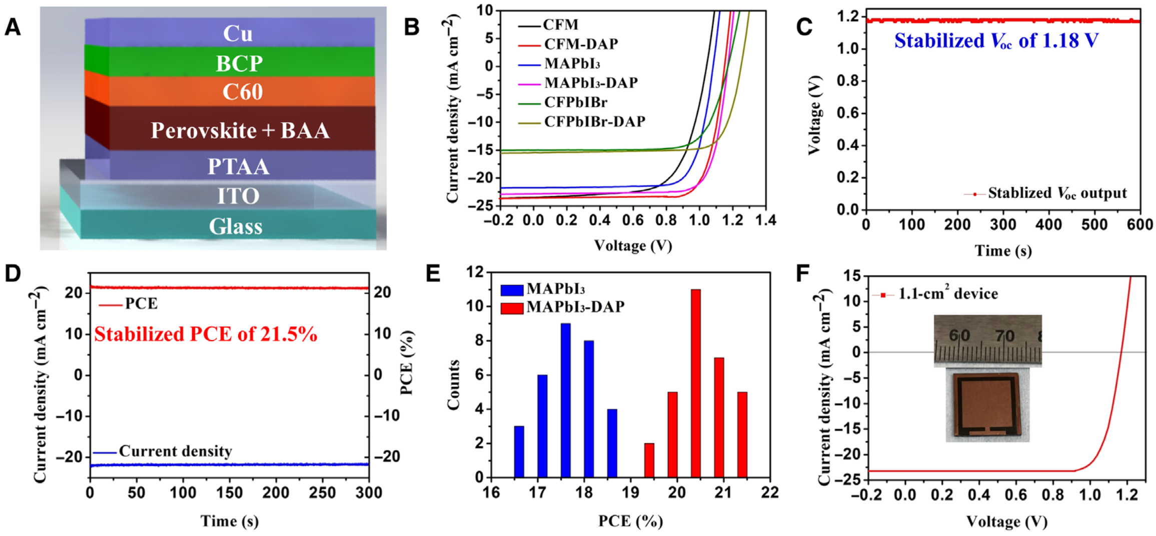

Fig. 3. Device structure and photovoltaic performance. (**A**) Schematic illustration of a completed PSC with inverted p-i-n device structure. (**B**) *J-V* curves of PSCs based on different perovskite compositions incorporated with or without DAP additive. (**C**) Stabilized V_{oc} of $MAPbI_3$-DAP device as a function of time. (**D**) Stabilized current density and PCE at the maximum power point (0.98 V) of the champion $MAPbI_3$-DAP device (0.08 cm^2). (**E**) PCE histogram of PSCs based on $MAPbI_3$ and $MAPbI_3$-DAP films (with 0.025 wt % DAP). (**F**) *J-V* characteristic of the champion 1.1 cm^2 PSC based on $MAPbI_3$-DAP thin film (inset shows a digital image of the actual device).

Table 1. Photovoltaic parameters of the PSCs using different perovskite layers prepared with various compositions and ink formulations under 1-sun illumination (AM1.5G, 100 mW cm^{-2}). Note that CFM has an optical bandgap of 1.51 eV, $MAPbI_3$ has an optical bandgap of 1.55 eV, and CFPbIBr has an optical bandgap of 1.82 eV. The optical bandgap of perovskite with different composition is determined from the external quantum efficiency (EQE) spectrum edge in figs. S11 to S13. Data for average PCE (η) were calculated from at least 30 devices. CFM represents $Cs_{0.05}FA_{0.70}MA_{0.25}PbI_3$ and CFPbIBr represents $Cs_{0.2}FA_{0.8}Pb(I_{0.6}Br_{0.4})_3$ (see details in Materials and Methods section).

PSCs	J_{sc}(mA cm^{-2})	V_{oc}(V)	η(%)	Average η(%)	FF(%)	V_{oc} deficit(V)
CFM	23.4	1.06	17.0	15.02 ± 0.78	68.4	0.45
CFM-DAP	23.4	1.16	21.5	20.36 ± 0.46	79.4	0.35
$MAPbI_3$	22.0	1.08	18.3	16.45 ± 0.40	77.2	0.47
$MAPbI_3$-DAP	22.5	1.18	21.7	20.53 ± 0.38	81.7	0.37
$MAPbI_3$-DAP (1.1 cm^2)	22.0	1.14	20.0	18.24 ± 0.65	80.0	N/A
CFPbIBr	15.1	1.18	13.1	11.78 ± 0.57	73.3	0.64
CFPbIBr-DAP	15.6	1.26	15.2	13.87 ± 0.49	77.5	0.56

$MAPbI_3$-DAP–based devices demonstrated the best performance among all tested perovskite compositions. The very high V_{oc} of 1.18 V for $MAPbI_3$-DAP device was confirmed by measuring the stabilized V_{oc} for 10 min (Fig. 3C). Specifically, this device had a low V_{oc} deficit of 0.37 eV, which is a record low value for all $MAPbI_3$-based PSCs reported to date, regardless of their fabrication methods. Figure S12 shows the EQE spectrum of the champion PSC based on the $MAPbI_3$-DAP thin film, in which the EQE profile exceeds 85% across a broad wavelength region from 450 to 750 nm. In addition, the integrated J_{sc} (22.0 mA cm^{-2}) from the EQE spectrum is in good agreement with that derived from the J-V curve (22.5 mA cm^{-2}), with a discrepancy of no more than 3%. Figure 3D depicts the stabilized J_{sc} of this champion device as measured at maximum power point of 0.98 V, giving a stabilized PCE of 21.5% under AM1.5G illumination. This highly stabilized PCE is among the best record for $MAPbI_3$-based PSCs, especially given that the devices in this work were fabricated using a scalable blade-coating method. The PCE histogram of $MAPbI_3$ and $MAPbI_3$-DAP–based PSCs were collected from a batch of 30 devices for each condition (Fig. 3E). Specifically, more than 77% of $MAPbI_3$-DAP PSCs had PCEs above 20.5%, while only 40% of $MAPbI_3$ devices had efficiencies over 18% under 1-sun illumination. This result not only demonstrates the effectiveness of improving the device performance but also highlights the excellent reproducibility of this BAA passivation strategy. We also fabricated larger area (>1 cm^2) PSCs using the bladed $MAPbI_3$-DAP films. The PSC with an aperture of 1.1 cm^2 shows a PCE of 20.0%, a J_{sc} of 22.0 mA cm^{-2}, a V_{oc} of 1.14 V, and an FF of 80% (Fig. 3F).

DISCUSSION

Passivation effect of DAP

Time-resolved photoluminescence (TRPL) lifetimes were measured for perovskite films with and without DAP incorporation. The $MAPbI_3$-DAP film had a PL recombination lifetime of 689 ns, almost 2.5 times longer than the control film (278 ns; Fig. 4A), at an excitation carrier concentration of 7.2×10^{13} cm^{-3}. Steady PL intensities of different perovskite films deposited on glass substrates are shown in fig. S14. DAP incorporation into perovskites of all compositions both enhanced the PL intensities and slightly blueshifted the PL peak. The PL results collectively confirm the defect passivation function induced by BAA incorporation.

To investigate the carrier recombination dynamics in the operating devices, we compared carrier recombination lifetimes of $MAPbI_3$ devices with or without DAP additive using transient photovoltage (TPV) measurements. The devices were soaked under 1-sun illumination, and laser pulses were applied to perturb the open-circuited devices and trigger a small transient photovoltaic signal (*35*). As seen in Fig. 4B, carrier recombination lifetime is longer in the $MAPbI_3$-DAP device (0.95 μs) compared to the pristine $MAPbI_3$ device (0.53 μs), suggesting that DAP amine passivation suppresses charge carrier recombination. This result is in good agreement with the enhanced V_{oc} in the $MAPbI_3$-DAP devices. The elongated carrier lifetime of PSCs with DAP passivation can be attributed to an effective reduction of trap densities within the perovskite films. The trap density of states (tDOS) for devices was measured using thermal admittance spectroscopy (TAS). Figure 4C showed reduced tDOS over the whole trap depth region for the $MAPbI_3$-DAP device. Specifically, the $MAPbI_3$-DAP device had one to two orders of magnitude lower tDOS than its $MAPbI_3$ counterpart, in both the deeper trap region (0.40 to 0.55 eV), which is assigned to defects at the film surface, and the shallower trap region (0.30 to 0.40 eV), which corresponded to traps at grain boundaries (*36*). This again confirms that the DAP amine can effectively passivate the defects originating from undercoordinated ions at the perovskite grain surface and further implies that the incorporation of BAA into the bulk and/or its presence at grain boundaries and surfaces during perovskite film formation is critical to the observed performance enhancement.

The light intensity–dependent V_{oc} shown in Fig. 4D provides more information on charge recombination in PSC devices. The diode ideal factor (n), which can be calculated ($n = kT/q \times \Delta V_{oc}/\Delta \ln J_L$, where k, T, q, and J_L are Boltzmann constant, absolute temperature, elementary charge, and photogenerated current density, respectively), is commonly used to describe the dependence of applied light intensity and voltage (*37*). The simulated lines were fitted from the light intensities higher than 0.01 sun. It has been reported that n can vary between 1 and 3 for PSCs, depending on the trap-assisted recombination (*38*, *39*). The $MAPbI_3$-DAP device exhibited a higher V_{oc} value than the $MAPbI_3$ device under all light intensities. The $MAPbI_3$ device had an ideal factor of 2.72, suggesting a severe impact of nonradiative recombination. In contrast, DAP passivation decreased the ideal factor to 1.43, much closer to that of an ideal diode, indicating that the nonradiative recombination process was effectively suppressed

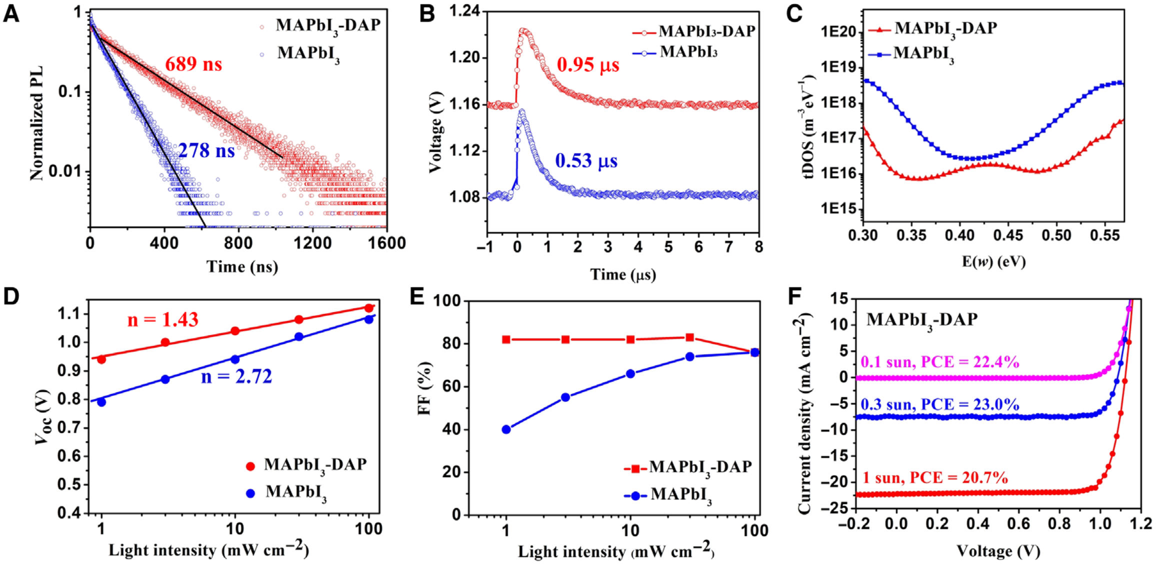

Fig. 4. Carrier recombination lifetime, trap densities, ideal factor, and weak light photovoltaic response. (**A**) TRPL of perovskite film incorporated with or without DAP amine. (**B**) Carrier recombination lifetime measured by transient photovoltage (TPV) and (**C**) trap density of states (tDOS) obtained from thermal admittance spectroscopy (TAS) measurement of PSCs with or without DAP passivation. (**D**) V_{oc} and (**E**) FF dependence as a function of light intensity. (**F**) *J-V* curves of PSCs based on MAPbI$_3$-DAP film measured under illumination at different light intensities.

due to the reduction of the surface defect states of perovskite film by DAP incorporation (*40*).

The influence of trap-assisted recombination on device performance is more evident for devices under weak light. Figure 4E compares the light intensity dependence of the FF for the two devices. Under weak light, the MAPbI$_3$ device displays a low FF, confirming the predominant nonradiative recombination process caused by deep-level trap states, whereas for the MAPbI$_3$-DAP device, the FF remains high, indicating that DAP passivation had effectively reduced trap-assisted recombination. This effect is also evidenced by a prolonged TPV lifetime of 1.7 μs for the MAPbI$_3$-DAP device, which is more than double that of the MAPbI$_3$ counterpart under 0.3-sun illumination (0.8 μs; fig. S15). The corollary of reduced charge recombination loss is higher V_{oc} and FF and thus high-efficiency of PSCs. As the light intensity decreased to low values, i.e., much lower than 0.01% sun, we observed a V_{oc} higher than 0.9 V for the MAPbI$_3$-DAP device, which is promising for indoor ambient light solar cell applications. The PCEs of devices with or without DAP passivation were measured under illumination at different light intensities (Fig. 4F and fig. S16). The MAPbI$_3$-DAP–based PSC (0.08 cm^2) had a PCE of 23.0% with a J_{sc} of 7.63 mA cm^{-2}, a V_{oc} of 1.08 V, an FF of 83.9%, and a stabilized PCE of 22.6% under 0.3-sun illumination (fig. S17), signifying that DAP amine–passivated PSCs are ideally suited for ambient light energy harvesting and conversion application (*41*, *42*).

Stability evaluation

Metal halide perovskites are notoriously sensitive to moisture and can degrade rapidly in a humid environment (*43*). The moisture stability of pristine MAPbI$_3$ film and DAP-modified MAPbI$_3$ film was studied by exposing them continuously to ambient air (relative humidity of 50 ± 5% at room temperature) for 120 hours. Under the same conditions, the MAPbI$_3$-DAP thin film maintained a highly pure MAPbI$_3$ phase without XRD-detectable PbI$_2$ phase, whereas decomposition from MAPbI$_3$ to PbI$_2$ was observed for the MAPbI$_3$ thin film (fig. S18). The shelf lifetime of completed devices without encapsulation was also tested at ambient conditions (50 ± 5 RH% at room temperature). As shown in Fig. 5A, the MAPbI$_3$ device degraded to 50% of its initial PCE after 500 hours, whereas the MAPbI$_3$-DAP device retained more than 90% of original PCE after storage for 1000 hours. In addition, the stability of encapsulated PSCs based on MAPbI$_3$ and MAPbI$_3$-DAP thin films under realistic operating conditions was measured. DAP incorporation enhanced the device stability under continuous 1-sun illumination, with the MAPbI$_3$-DAP device retaining 90% of initial PCE after 500 hours. In contrast, the PCE of MAPbI$_3$ device decreased with prolonged illumination duration to only 35% of original PCE after 200 hours (Fig. 5B). Last, the thermal stability of the PSCs with DAP passivation was evaluated, in which the devices were heated to 85°C inside a N$_2$-filled glove box. As is shown in fig. S19, there is almost no PCE reduction for the MAPbI$_3$-DAP device after being heated for 24 hours. Such good thermal stability, in turn, confirms that the DAP still binds quite strongly to the perovskites after heat treatment. The low boiling point of DAP only indicates the weak interaction of amine molecules themselves in a liquid form. After the formation of bonding between DAP and perovskites, the amine itself is not liquid anymore and thus exists as a robust defect passivation agent within perovskite films. The significantly enhanced moisture and operational stability of MAPbI$_3$-DAP–based PSCs demonstrates the beneficial effect of DAP amine incorporation. In addition, the self-assembly of a moisture barrier via the additive-assisted perovskite film blade coating warrants to effectively retard the decomposition of perovskites under atmospheric conditions. The improved ambient and operational stability could be attributed to synergistic functions of the DAP amine. On one hand, DAP may shield the surface and interior of perovskite grains from moisture. On the other hand, DAP could passivate the undercoordinated ions at the boundaries and surfaces of perovskite grains, thus alleviating the defect-induced degradation that normally occurs under operating conditions.

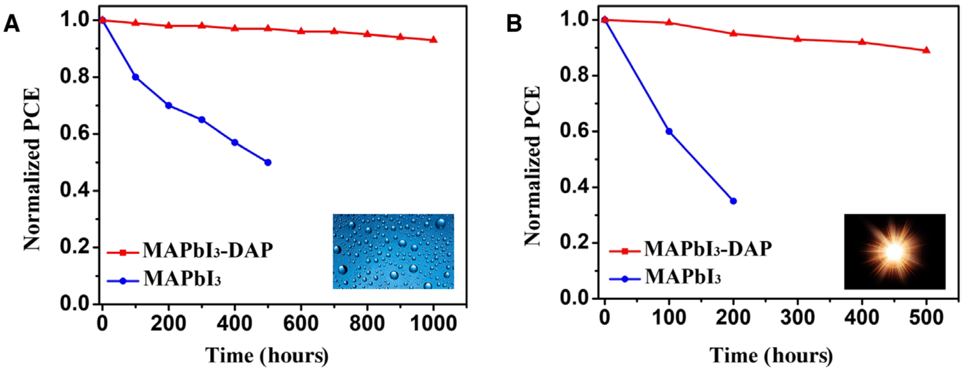

Fig. 5. Stability test. (**A**) Moisture stability of nonencapsulated PSCs based on $MAPbI_3$-DAP and $MAPbI_3$ films under ambient air (50 ± 5 RH% at room temperature). (**B**) Operational stability of encapsulated PSCs based on $MAPbI_3$-DAP and $MAPbI_3$ films under continuous 1-sun illumination.

CONCLUSIONS

We demonstrated the incorporation of BAA additives into a perovskite ink for scalable fabrication of efficient and stable PSCs. PSCs incorporated with DAP showed impressive PCEs of up to 21.7% with an aperture area of 0.08 cm^2 (stabilized output exceeding 21.5%) and 20% over 1.1 cm^2, which can be attributed to the effective passivation of undercoordinated ions within perovskite films. Compared with other reported inorganic/organic additives, which were all used in spin-coated devices, the BAA additive not only yields a record PCE but is also compatible with the blade-coating process. The BAA additive exhibits fascinating multifunctionalities, including perovskite crystal growth modulation, reinforced grain boundaries, a self-assembled moisture barrier, and stabilized undercoordinated ions, which all played critical roles in improving the efficiency and the ambient and operational stability of the blade-coated devices. The concept of bilateral amine passivation and functionalization can be universally applied to other mixed-cation and mixed-halide perovskites, thus offering an effective pathway toward fabricating large-scale halide perovskite devices with superior performance and improved stability.

MATERIALS AND METHODS

Materials

Unless stated otherwise, all materials and solvents were purchased from Sigma-Aldrich. Lead iodide (PbI_2, 99.999%) was purchased from Alfa Aesar. MAI was purchased from GreatCell Solar. All chemicals were used as received without further purification.

Device fabrication

The ITO glass substrates were cleaned using an ultrasonicator in deionized water, acetone, and an isopropanol bath for 30 min successively and subjected to UV-ozone treatment for 15 min. A PTAA layer was deposited on the ITO glass by blade coating the PTAA/toluene solution (5 mg ml^{-1}) at a speed of 15 mm s^{-1} and by annealing at 70°C for 10 min. The gap between the blade coater and the substrate was controlled at 100 μm. Five microliters of solution was used for coating PTAA on a 1.5 cm by 1.5 cm ITO substrate. The blade coating of perovskite layer was adjusted from a previous method (*7*). Specifically, the 1.1 M $MAPbI_3$ perovskite ink was prepared by dissolving 1.1 M PbI_2 and 1.1 M MAI in 1-ml *N,N'*-dimethylformamide (DMF). Other perovskite inks with different compositions, $Cs_{0.05}FA_{0.70}MA_{0.25}PbI_3$ (CFM; with a bandgap of 1.51 eV) and $Cs_{0.2}FA_{0.8}Pb(I_{0.6}Br_{0.4})_3$ (CFPbIBr; with a bandgap of 1.82 eV), were prepared for comparison. Before use, small amounts of additives, i.e., methylammonium hypophosphite (0.15 wt %) and L-α-phosphatidylcholine (0.05 wt %), were added to achieve uniform coating of perovskite film with good surface coverage (*6*). A series of BAA additives, including DAP, DAH, and DAO, were dissolved in DMF separately and then added to the as-prepared perovskite ink at an optimized concentration of 0.025 wt %. Precursor ink (5 to 10 μl) was dripped onto the ITO substrate, which was set on a hot plate at 150°C, and then swiped linearly by a film applicator at a speed of 7.5 mm s^{-1}. After coating, the perovskite films were annealed at 100°C for 10 min. The blade coating of both PTAA layers and perovskite films was conducted in a N_2-purged glove box (below 1.0 parts per million of O_2 and H_2O). Last, 25 nm of C_{60} (Nano-C), 8 nm of BCP, and 80 nm of Cu electrode were sequentially deposited by thermal evaporation to form a complete PSC device.

Device characterization

SEM images were taken by a Quanta 200 field-emission gun environmental SEM. XRD patterns were obtained with a Bruker D8 Discover diffractometer with Cu Kα radiation (1.5406 Å). The *J-V* measurement of the devices (voltage scanning rate 0.1 V s^{-1}) and the steady photocurrent under maximum power output bias (0.98 V) were recorded with a Keithley 2400 SourceMeter under simulated AM1.5G irradiation produced by a Xenon lamp–based solar simulator (Oriel Sol3A Class AAA Solar Simulator). The light intensity was calibrated by a silicon reference cell equipped with a SCHOTT visible color KG5 glass filter (Newport 91150V). A nonreflective shadow mask was used to define the active area of the PSCs. EQE spectra were obtained by a Newport QE measurement kit by focusing a monochromatic light beam with wavelength from 300 to 900 nm onto the devices. PL spectrum was measured with a Horiba iHR320 imaging spectrometer at room temperature. A 532-nm green laser (Laserglow Technologies) with an intensity of 100 mW cm^{-2} was used as the excitation source. TRPL was obtained using a DeltaPro time-correlated single photon counting (TCSPC) filter fluorometer with a pulsed laser source at 406 nm (Horiba NanoLED 402-LH; pulse width below 200 ps, 20 pJ per pulse, approximately 1-mm^2 spot size), and the signal was recorded using TCSPC. AFM measurement was conducted on an Asylum Research MFP-3D AFM. TPV decay was measured under different light intensities and recorded by a 1-GHz Agilent digital oscilloscope. The FTIR spectra (4000 to 500 cm^{-1}) were recorded on a PerkinElmer

FTIR spectrometer with powders scratched from several pieces of samples.

SUPPLEMENTARY MATERIALS

Supplementary material for this article is available at http://advances.sciencemag.org/cgi/content/full/5/3/eaav8925/DC1

Fig. S1. FTIR measurement of amine-incorporated perovskite material.
Fig. S2. XRD patterns of perovskite films before annealing.
Fig. S3. Variation of $MAPbI_3$ film morphology with increasing DAP contents.
Fig. S4. Effect of different amounts of DAP on perovskite crystal orientation.
Fig. S5. Surface roughness of perovskite films.
Fig. S6. Dark current measurement.
Fig. S7. Energy diagram of PSC device.
Fig. S8. Perovskite film thickness and quality.
Fig. S9. Hysteresis study.
Fig. S10. Lateral device architecture and its current response.
Fig. S11. EQE measurement of CFM device.
Fig. S12. EQE measurement of the champion $MAPbI_3$-DAP device.
Fig. S13. EQE measurement of CFPbIBr-DAP device.
Fig. S14. Steady PL measurement of perovskite films with different compositions.
Fig. S15. Carrier recombination lifetime.
Fig. S16. Light intensity–dependent *J-V* performances.
Fig. S17. Stabilized PCE output.
Fig. S18. Perovskite films degradation in ambient air.
Fig. S19. Thermal stability test.
Table S1. Summarized work functions, valence band maximum (VBM), and conduction band minimum (CBM) positions for different functional layers in the PSCs.
Table S2. Photovoltaic parameters of PSCs using bladed $MAPbI_3$ films incorporated with different amounts of DAP amine additives.
Table S3. Photovoltaic parameters of PSCs based on $MAPbI_3$-DAP film measured under AM1.5G illumination in different scan directions.

REFERENCES AND NOTES

1. W. S. Yang, B.-W. Park, E. H. Jung, N. J. Jeon, Y. C. Kim, D. U. Lee, S. S. Shin, J. Seo, E. K. Kim, J. H. Noh, S. I. Seok, Iodide management in formamidinium-lead-halide–based perovskite layers for efficient solar cells. *Science* **356**, 1376–1379 (2017).
2. M. Yang, Z. Li, M. O. Reese, O. G. Reid, D. H. Kim, S. Siol, T. R. Klein, Y. Yan, J. J. Berry, M. F. A. M. van Hest, K. Zhu, Perovskite ink with wide processing window for scalable high-efficiency solar cells. *Nat. Energy* **2**, 17038 (2017).
3. Z. Li, T. R. Klein, D. H. Kim, M. Yang, J. J. Berry, M. F. A. M. van Hest, K. Zhu, Scalable fabrication of perovskite solar cells. *Nat. Rev. Mater.* **3**, 18017 (2018).
4. Y. Hou, X. Du, S. Scheiner, D. P. McMeekin, Z. Wang, N. Li, M. S. Killian, H. Chen, M. Richter, I. Levchuk, N. Schrenker, E. Spiecker, T. Stubhan, N. A. Luechinger, A. Hirsch, P. Schmuki, H.-P. Steinrück, R. H. Fink, M. Halik, H. J. Snaith, C. J. Brabec, A generic interface to reduce the efficiency-stability-cost gap of perovskite solar cells. *Science* **358**, 1192–1197 (2017).
5. S. Tang, Y. Deng, X. Zheng, Y. Bai, Y. Fang, Q. Dong, H. Wei, J. Huang, Composition engineering in doctor-blading of perovskite solar cells. *Adv. Energy Mater.* **7**, 1700302 (2017).
6. Y. Deng, X. Zheng, Y. Bai, Q. Wang, J. Zhao, J. Huang, Surfactant-controlled ink drying enables high-speed deposition of perovskite films for efficient photovoltaic modules. *Nat. Energy* **3**, 560–566 (2018).
7. W.-Q. Wu, Q. Wang, Y. Fang, Y. Shao, S. Tang, Y. Deng, H. Lu, Y. Liu, T. Li, Z. Yang, A. Gruverman, J. Huang, Molecular doping enabled scalable blading of efficient hole-transport-layer-free perovskite solar cells. *Nat. Commun.* **9**, 1625 (2018).
8. F. Huang, A. R. Pascoe, W.-Q. Wu, Z. Ku, Y. Peng, J. Zhong, R. A. Caruso, Y.-B. Cheng, Effect of the microstructure of the functional layers on the efficiency of perovskite solar cells. *Adv. Mater.* **29**, 1601715 (2017).
9. W.-Q. Wu, D. Chen, W. A. McMaster, Y.-B. Cheng, R. A. Caruso, Solvent-mediated intragranular-coarsening of $CH_3NH_3PbI_3$ thin films toward high-performance perovskite photovoltaics. *ACS Appl. Mater. Interfaces* **9**, 31959–31967 (2017).
10. W.-Q. Wu, D. Chen, F. Huang, Y.-B. Cheng, R. A. Caruso, Optimizing semiconductor thin films with smooth surfaces and well-interconnected networks for high-performance perovskite solar cells. *J. Mater. Chem. A* **4**, 12463–12470 (2016).
11. X. Zheng, B. Chen, J. Dai, Y. Fang, Y. Bai, Y. Lin, H. Wei, X. C. Zeng, J. Huang, Defect passivation in hybrid perovskite solar cells using quaternary ammonium halide anions and cations. *Nat. Energy* **2**, 17102 (2017).
12. H. Jiang, Z. Yan, H. Zhao, S. Yuan, Z. Yang, J. Li, B. Liu, T. Niu, J. Feng, Q. Wang, D. Wang, H. Yang, Z. Liu, S. F. Liu, Bifunctional hydroxylamine hydrochloride incorporated perovskite films for efficient and stable planar perovskite solar cells. *ACS Appl. Energy Mater.* **1**, 900–909 (2018).
13. Y. Deng, E. Peng, Y. Shao, Z. Xiao, Q. Dong, J. Huang, Scalable fabrication of efficient organolead trihalide perovskite solar cells with doctor-bladed active layers. *Energ. Environ. Sci.* **8**, 1544–1550 (2015).
14. T. Leijtens, G. E. Eperon, N. K. Noel, S. N. Habisreutinger, A. Petrozza, H. J. Snaith, Stability of metal halide perovskite solar cells. *Adv. Energy Mater.* **5**, 1500963 (2015).
15. T. Liu, Y. Zhou, Z. Li, L. Zhang, M.-G. Ju, D. Luo, Y. Yang, M. Yang, D. H. Kim, W. Yang, N. P. Padture, M. C. Beard, X. C. Zeng, K. Zhu, Q. Gong, R. Zhu, Stable formamidinium-based perovskite solar cells via in situ grain encapsulation. *Adv. Energy Mater.* **8**, 1800232 (2018).
16. Y. Bai, Q. Dong, Y. Shao, Y. Deng, Q. Wang, L. Shen, D. Wang, W. Wei, J. Huang, Enhancing stability and efficiency of perovskite solar cells with crosslinkable silane-functionalized and doped fullerene. *Nat. Commun.* **7**, 12806 (2016).
17. D. Bi, P. Gao, R. Scopelliti, E. Oveisi, J. Luo, M. Grätzel, A. Hagfeldt, M. K. Nazeeruddin, High-performance perovskite solar cells with enhanced environmental stability based on amphiphile-modified $CH_3NH_3PbI_3$. *Adv. Mater.* **28**, 2910–2915 (2016).
18. F. Wang, W. Geng, Y. Zhou, H.-H. Fang, C.-J. Tong, M. A. Loi, L.-M. Liu, N. Zhao, Phenylalkylamine passivation of organolead halide perovskites enabling high-efficiency and air-stable photovoltaic cells. *Adv. Mater.* **28**, 9986–9992 (2016).
19. X. Liu, Y. Zhang, L. Shi, Z. Liu, J. Huang, J. S. Yun, Y. Zeng, A. Pu, K. Sun, Z. Hameiri, J. A. Stride, J. Seidel, M. A. Green, X. Hao, Exploring inorganic binary alkaline halide to passivate defects in low-temperature-processed planar-structure hybrid perovskite solar cells. *Adv. Energy Mater.* **8**, 1800138 (2018).
20. P.-W. Liang, C.-Y. Liao, C.-C. Chueh, F. Zuo, S. T. Williams, X.-K. Xin, J. Lin, A. K.-Y. Jen, Additive enhanced crystallization of solution-processed perovskite for highly efficient planar-heterojunction solar cells. *Adv. Mater.* **26**, 3748–3754 (2014).
21. Y. Wu, F. Xie, H. Chen, X. Yang, H. Su, M. Cai, Z. Zhou, T. Noda, L. Han, Thermally stable $MAPbI_3$ perovskite solar cells with efficiency of 19.19% and area over 1 cm^2 achieved by additive engineering. *Adv. Mater.* **29**, 1701073 (2017).
22. T. Zhang, M. I. Dar, G. Li, F. Xu, N. Guo, M. Grätzel, Y. Zhao, Bication lead iodide 2D perovskite component to stabilize inorganic α-$CsPbI_3$ perovskite phase for high-efficiency solar cells. *Sci. Adv.* **3**, e1700841 (2017).
23. Z. Wang, Q. Lin, F. P. Chmiel, N. Sakai, L. M. Herz, H. J. Snaith, Efficient ambient-air-stable solar cells with 2D–3D heterostructured butylammonium-caesium-formamidinium lead halide perovskites. *Nat. Energy* **2**, 17135 (2017).
24. J. Lu, L. Jiang, W. Li, F. Li, N. K. Pai, A. D. Scully, C.-M. Tsai, U. Bach, A. N. Simonov, Y.-B. Cheng, L. Spiccia, Diammonium and monoammonium mixed-organic-cation perovskites for high performance solar cells with improved stability. *Adv. Energy Mater.* **7**, 1700444 (2017).
25. L. Zuo, H. Guo, D. W. deQuilettes, S. Jariwala, N. De Marco, S. Dong, R. DeBlock, D. S. Ginger, B. Dunn, M. Wang, Y. Yang, Polymer-modified halide perovskite films for efficient and stable planar heterojunction solar cells. *Sci. Adv.* **3**, e1700106 (2017).
26. Y. Zong, Y. Zhou, Y. Zhang, Z. Li, L. Zhang, M.-G. Ju, M. Chen, S. Pang, X. C. Zeng, N. P. Padture, Continuous grain-boundary functionalization for high-efficiency perovskite solar cells with exceptional stability. *Chem* **4**, 1404–1415 (2018).
27. D. Bi, C. Yi, J. Luo, J.-D. Décoppet, F. Zhang, S. M. Zakeeruddin, X. Li, A. Hagfeldt, M. Grätzel, Polymer-templated nucleation and crystal growth of perovskite films for solar cells with efficiency greater than 21%. *Nat. Energy* **1**, 16142 (2016).
28. J.-Y. Seo, T. Matsui, J. Luo, J.-P. Correa-Baena, F. Giordano, M. Saliba, K. Schenk, A. Ummadisingu, K. Domanski, M. Hadadian, A. Hagfeldt, S. M. Zakeeruddin, U. Steiner, M. Grätzel, A. Abate, Ionic liquid control crystal growth to enhance planar perovskite solar cells efficiency. *Adv. Energy Mater.* **6**, 1600767 (2016).
29. T. Suksrichavalit, S. Prachayasittikul, C. Nantasenamat, C. Isarankura-Na-Ayudhya, V. Prachayasittikul, Copper complexes of pyridine derivatives with superoxide scavenging and antimicrobial activities. *Eur. J. Med. Chem.* **44**, 3259–3265 (2009).
30. N. F. Curtis, Macrocyclic coordination compounds formed by condensation of metal-amine complexes with aliphatic carbonyl compounds. *Coord. Chem. Rev.* **3**, 3–47 (1968).
31. T. Baikie, Y. Fang, J. M. Kadro, M. Schreyer, F. Wei, S. G. Mhaisalkar, M. Graetzel, T. J. White, Synthesis and crystal chemistry of the hybrid perovskite $(CH_3NH_3)PbI_3$ for solid-state sensitised solar cell applications. *J. Mater. Chem. A* **1**, 5628–5641 (2013).
32. L. N. Quan, M. Yuan, R. Comin, O. Voznyy, E. M. Beauregard, S. Hoogland, A. Buin, A. R. Kirmani, K. Zhao, A. Amassian, D. H. Kim, E. H. Sargent, Ligand-stabilized reduced-dimensionality perovskites. *J. Am. Chem. Soc.* **138**, 2649–2655 (2016).
33. Y. Yuan, T. Li, Q. Wang, J. Xing, A. Gruverman, J. Huang, Anomalous photovoltaic effect in organic-inorganic hybrid perovskite solar cells. *Sci. Adv.* **3**, e1602164 (2017).
34. M. U. Rothmann, W. Li, Y. Zhu, A. Liu, Z. Ku, U. Bach, J. Etheridge, Y.-B. Cheng, Structural and chemical changes to $CH_3NH_3PbI_3$ induced by electron and gallium ion beams. *Adv. Mater.* **30**, 1800629 (2018).
35. Q. Wang, Q. Dong, T. Li, A. Gruverman, J. Huang, Thin insulating tunneling contacts for efficient and water-resistant perovskite solar cells. *Adv. Mater.* **28**, 6734–6739 (2016).

36. Y. Shao, Z. Xiao, C. Bi, Y. Yuan, J. Huang, Origin and elimination of photocurrent hysteresis by fullerene passivation in $CH_3NH_3PbI_3$ planar heterojunction solar cells. *Nat. Commun.* **5**, 5784 (2014).
37. M. Bernechea, N. C. Miller, G. Xercavins, D. So, A. Stavrinadis, G. Konstantatos, Solution-processed solar cells based on environmentally friendly $AgBiS_2$ nanocrystals. *Nat. Photonics* **10**, 521–525 (2016).
38. T. Singh, T. Miyasaka, Stabilizing the efficiency beyond 20% with a mixed cation perovskite solar cell fabricated in ambient air under controlled humidity. *Adv. Energy Mater.* **8**, 1700677 (2018).
39. C. Fei, B. Li, R. Zhang, H. Fu, J. Tian, G. Cao, Highly efficient and stable perovskite solar cells based on monolithically grained $CH_3NH_3PbI_3$ film. *Adv. Energy Mater.* **7**, 1602017 (2017).
40. M. Stolterfoht, C. M. Wolff, Y. Amir, A. Paulke, L. Perdigón-Toro, P. Caprioglio, D. Neher, Approaching the fill factor Shockley–Queisser limit in stable, dopant-free triple cation perovskite solar cells. *Energ. Environ. Sci.* **10**, 1530–1539 (2017).
41. M. Freitag, J. Teuscher, Y. Saygili, X. Zhang, F. Giordano, P. Liska, J. Hua, S. M. Zakeeruddin, J.-E. Moser, M. Grätzel, A. Hagfeldt, Dye-sensitized solar cells for efficient power generation under ambient lighting. *Nat. Photonics* **11**, 372–378 (2017).
42. Y. Cao, Y. Liu, S. M. Zakeeruddin, A. Hagfeldt, M. Grätzel, Direct contact of selective charge extraction layers enables high-efficiency molecular photovoltaics. *Joule* **2**, 1108–1117 (2018).
43. X. Li, M. Ibrahim Dar, C. Yi, J. Luo, M. Tschumi, S. M. Zakeeruddin, M. K. Nazeeruddin, H. Han, M. Grätzel, Improved performance and stability of perovskite solar cells by crystal crosslinking with alkylphosphonic acid ω-ammonium chlorides. *Nat. Chemistry* **7**, 703–711 (2015).

Acknowledgments

Funding: This work was financially supported by the Office of Naval Research under awards N00014-17-1-2619 and N00014-17-1-2727 and the Air Force Office of Scientific Research (AFOSR) (grant no. A9550-16-1-0299). **Author contributions:** J.H. and W.-Q.W. conceived the idea. W.-Q.W. conducted most of device fabrication, measurement, and characterization. Z.Y. and H.W. contributed to the ideality factor study; P.N.R. conducted the film morphology SEM study; J.Z. conducted the XRD measurements; Y.S. and Y. Fang carried out the TRPL study; X.D. conducted the AFM and trap density studies; X.X. and Y. Feng carried out the carrier lifetime study, and Y.L., Q.W. and Y.D. contributed to the FTIR study and morphology analysis. J.H. and W.-Q.W. wrote the manuscript. All authors discussed the results and commented on the manuscript. **Competing interests:** The authors declare that they have no competing interests. **Data and materials availability:** All data needed to evaluate the conclusions in the paper are present in the paper and/or the Supplementary Materials. Additional data related to this paper may be requested from J.H. (jhuang@unc.edu).

Submitted 30 October 2018
Accepted 28 January 2019
Published 8 March 2019
10.1126/sciadv.aav8925

Citation: W.-Q. Wu, Z. Yang, P. N. Rudd, Y. Shao, X. Dai, H. Wei, J. Zhao, Y. Fang, Q. Wang, Y. Liu, Y. Deng, X. Xiao, Y. Feng, J. Huang, Bilateral alkylamine for suppressing charge recombination and improving stability in blade-coated perovskite solar cells. *Sci. Adv.* **5**, eaav8925 (2019).